PCCP

PAPER

View Article Online
View Journal | View Issue

Cite this: *Phys. Chem. Chem. Phys.*, 2017, **19**, 20867

Size dependent behavior of Fe_3O_4 crystals during electrochemical (de)lithiation: an *in situ* X-ray diffraction, *ex situ* X-ray absorption spectroscopy, transmission electron microscopy and theoretical investigation†

David C. Bock,‡[a] Christopher J. Pelliccione,‡[a] Wei Zhang,[a] Janis Timoshenko,[b] K. W. Knehr,[c] Alan C. West,[c] Feng Wang,[a] Yan Li,[d] Anatoly I. Frenkel,[b] Esther S. Takeuchi, *[abe] Kenneth J. Takeuchi*[be] and Amy C. Marschilok *[be]

Received 17th May 2017,
Accepted 17th July 2017

DOI: 10.1039/c7cp03312e

rsc.li/pccp

The iron oxide magnetite, Fe_3O_4, is a promising conversion type lithium ion battery anode material due to its high natural abundance, low cost and high theoretical capacity. While the close packing of ions in the inverse spinel structure of Fe_3O_4 enables high energy density, it also limits the kinetics of lithium ion diffusion in the material. Nanosizing of Fe_3O_4 to reduce the diffusion path length is an effective strategy for overcoming this issue and results in improved rate capability. However, the impact of nanosizing on the multiple structural transformations that occur during the electrochemical (de)lithiation reaction in Fe_3O_4 is poorly understood. In this study, the influence of crystallite size on the lithiation-conversion mechanisms in Fe_3O_4 is investigated using complementary X-ray techniques along with transmission electron microscopy (TEM) and continuum level simulations on electrodes of two different Fe_3O_4 crystallite sizes. *In situ* X-ray diffraction (XRD) measurements were utilized to track the changes to the crystalline phases during (de)lithiation. X-ray absorption spectroscopy (XAS) measurements at multiple points during the (de)lithiation processes provided local electronic and atomic structural information. Tracking the crystalline and nanocrystalline phases during the first (de)lithiation provides experimental evidence that (1) the lithiation mechanism is non-uniform and dependent on crystallite size, where increased Li^+ diffusion length in larger crystals results in conversion to Fe^0 metal while insertion of Li^+ into spinel-Fe_3O_4 is still occurring, and (2) the disorder and size of the Fe metal domains formed when either material is fully lithiated impacts the homogeneity of the FeO phase formed during the subsequent delithiation.

Introduction

Magnetite (Fe_3O_4) is a promising electrode material for the next generation of lithium ion battery systems due to its low toxicity, low cost, and high specific capacity (*ca.* 924 mA h g^{-1}) arising from multiple electron transfer reactions.[1] Fe_3O_4 has an inverse-spinel structure, with Fe^{3+} ions partially occupying tetrahedral (8a) sites and other Fe^{3+} along with Fe^{2+} occupying octahedral (16d) sites in a cubic close packed array of O^{2-} ions.[2] The lithiation process during the first cycle in Fe_3O_4 has been investigated using X-ray diffraction (XRD),[3–7] indicating that initial lithiation proceeds *via* insertion resulting in $Li_xFe_3O_4$ ($0 < x < 2$), a rock salt like phase,[3–6] and ultimately conversion to Li_2O and Fe metal,[3] as also supported by recent X-ray absorption spectroscopy (XAS) and TEM studies.[8,9] However, there is limited literature regarding the structural changes occurring in the lithiated electrodes upon subsequent delithiation,[9] which is crucial information for complete understanding of the electrochemical behavior of Fe_3O_4.

While the close packing of ions in Fe_3O_4 enhances energy density, it can be detrimental to the lithium ion transport process. Lithium ion transport kinetics are expected to be the

[a] *Energy Sciences Directorate, Brookhaven National Laboratory, Upton, NY 11973, USA*
[b] *Department of Materials Science and Chemical Engineering, Stony Brook University, Stony Brook, NY 11974, USA. E-mail: esther.takeuchi@stonybrook.edu, kenneth.takeuchi.1@stonybrook.edu, amy.marschilok@stonybrook.edu*
[c] *Department of Chemical Engineering, Columbia University, New York, NY 10027, USA*
[d] *American Physical Society, Ridge, NY 11961, USA*
[e] *Department of Chemistry, Stony Brook University, Stony Brook, NY 11974, USA*

† Electronic supplementary information (ESI) available: Rietveld analysis of *in situ* XRD, full EXAFS fitting results. See DOI: 10.1039/c7cp03312e

‡ These two authors contributed equally to this work.

rate-limiting factor in the electrochemical reaction, since Fe_3O_4 has a sufficiently high electronic conductivity ($2 \times 10\ \Omega^{-1}\ m^{-1}$).[10] Nanosizing has been utilized as means of shortening the lithium ion diffusion path length in Fe_3O_4, improving rate capability and increasing utilization of the active material.[8,11–20] Furthermore, the use of conductive polymers has been found to enhance conductivity between active material particles, resulting in improved performance.[21–24] Despite these advances, however, ion transport limitations still exist during the initial insertion process, especially in larger nanocrystallites (*ca.* 30 nm).[25] Within the rock salt like phase and during the later conversion process to form iron metal, the prevalence of transport limitations and the impact of structure on transport is not well understood. Furthermore, limited literature exists regarding the structural changes that occur in the lithiated electrodes upon subsequent delithiation,[9] which is crucial information for complete understanding of the electrochemical behavior of Fe_3O_4. Thus, a detailed analysis of the dependence of electrochemically induced structural changes on Fe_3O_4 crystallite during (de)lithiation processes is warranted to fully comprehend the impact of nanosizing on the kinetics of lithium ion transport.

Due to the complexity of electrochemical reactions in Fe_3O_4 electrodes involving both insertion and conversion processes, understanding of the intricate structural changes occurring within the material benefits from the use of multiple characterization techniques.[26] X-ray diffraction (XRD) is an excellent method when studying crystalline materials, facilitating observations of changes in the crystal lattice, crystallite size as well as identification of new crystalline phases that may evolve during battery operation.[27–29] However, when the battery electrode material becomes amorphous or sufficiently nanocrystalline, structural information obtained from XRD can be limited.[30–32] X-ray absorption spectroscopy (XAS) in contrast is an element specific technique that can be utilized to study the local structure (within *ca.* 6 Å) around all specific metal elements within the sample. XAS, specifically X-ray absorption near-edge structure (XANES) and extended X-ray absorption fine structure (EXAFS) spectroscopies, can determine both local electronic and atomic structural information respectively. XAS has proven to be a powerful technique to investigate battery materials in a variety of complex lithium ion battery electrode systems.[33–35] Thus, the utilization of both XRD and XAS has shown to be an important combination to gain a more comprehensive understanding of the structural changes occurring in crystalline and amorphous/nanocrystalline phases in battery materials.[36–38]

In this study, *in situ* XRD using a laboratory Cu Kα radiation source, combined with synchrotron *ex situ* XAS measurements at the Fe K-edge and *ex situ* scanning transmission electron microscopy (STEM) images facilitated a thorough structural characterization of the (de)lithiation process in electrodes of two different Fe_3O_4 crystallite sizes as anodes for lithium ion batteries. In particular, the variations in structural changes around iron atoms as a function of lithium insertion/removal are correlated to observed electrochemistry. Tracking the crystalline and nanocrystalline phases during the first (de)lithiation in two different Fe_3O_4 crystallite sizes provides experimental evidence for several significant findings: (1) the lithiation mechanism is non-uniform and dependent on crystallite size, where increased Li^+ diffusion length in larger crystals results in conversion to Fe^0 metal while insertion of Li^+ into spinel-Fe_3O_4 is still occurring, and (2) the disorder of the Fe metal domains formed when either material is fully lithiated impacts the homogeneity of the FeO phase formed during the subsequent delithiation.

Experimental

Synthesis and characterization

A previously reported co-precipitation method[17,18] was used to synthesize Fe_3O_4 with crystallite size of *ca.* 11 nm. Fe_3O_4 of larger size (*ca.* 39 nm) was purchased through Alfa Aesar. Synthesized and commercially obtained Fe_3O_4 materials are denoted Fe_3O_4-S and Fe_3O_4-C, respectively. The pristine materials were identified by X-ray powder diffraction (XRD) using a Rigaku Miniflex diffractometer, equipped with a D/teX 1D silicon strip detector. The XRD data were measured in a 2θ range of 5 to 90° with a step width of 0.02° and a scan rate of $5^\circ\ min^{-1}$. Patterns were indexed to the reported Fe_3O_4 reference pattern (PDF #01-088-0315). Isotropic crystallite sizes size of the samples were determined *via* Rietveld refinement performed using the GSAS II software package.[39] Multipoint BET (Brunauer, Emmett, Teller) surface area data were collected using a Quantachrome Nova 4200e instrument on both Fe_3O_4-S and *ca.* Fe_3O_4-C nanoparticles using N_2(g) as adsorbent.

Electrochemistry

Fe_3O_4 electrode coatings were prepared on copper foil substrates with a 80 : 10 : 10 ratio of Fe_3O_4 : acetylene black carbon : polyvinylidene fluoride binder (PVDF). Resulting electrodes were used as the cathode in coin-type electrochemical cells with lithium metal anodes, polypropylene separators, and 1 M $LiPF_6$ in 30 : 70 ethylene carbonate : dimethyl carbonate electrolyte. Coin cells were delithiated and lithiated at a 0.1C current rate to various dis(delithiation) and cycled states for further XAS analysis. Specifically, Fe_3O_4-S electrodes were lithiated to 1 e^-, 2 e^-, 4 e^-, 6 e^-, 8 e^-, or 0.2 V (fully lithiated) then delithiated to 2 e^-, 4 e^- or 3.0 V (fully delithiated). Fe_3O_4-C electrodes were lithiated to 4 e^- and 0.2 V (fully lithiated) then delithiated to 4 e^- and 3.0 V (fully delithiated).

In situ XRD

In situ XRD diffraction patterns were acquired from both Fe_3O_4-S and Fe_3O_4-C electrodes by utilizing a novel vacuum-sealed plastic pouch electrochemical cell positioned within a Rigaku Miniflex diffractometer with Cu Kα radiation source, equipped with a D/teX 1D silicon strip detector to enable high-resolution XRD diffraction patterns with minimal data collection time. The pouch cells were secured within a specially designed sample holder to ensure proper sample height and alignment with respect to the incident X-rays and detector, leading to accurate measurements of 2θ. XRD scans were continuously collected in a 2θ range of 25–70° with step size of 0.03° and a scan rate

of 3° min^{-1} for the Fe_3O_4-C electrode and 2° min^{-1} for the Fe_3O_4-S electrode. All measurements were conducted in a low humidity dry room environment. After an initial XRD scan at open-circuit voltage (OCV) the pouch cell was lithiated and delithiated at 0.1C rate using a Bio-Logic multichannel potentiostat/galvanostat. After data acquisition, the XRD scans were correlated to the electrochemistry of the cell by comparing time-stamps of the electrochemical data and XRD scans respectively.

Performance modeling

The electrochemical experiments used to generate the *in situ* diffraction data with Fe_3O_4-S and Fe_3O_4-C were simulated using a previously published, multi-scale model.[25] This continuum-level model simulates the electrochemistry of a single agglomerate of nanocrystals by coupling ion diffusion on both length scales (agglomerate and crystal) with descriptions of the thermodynamics and reaction kinetics.

Ex situ X-ray absorption spectroscopy

Fe_3O_4 electrodes were removed from coin cell testing at specific electron equivalents during initial lithiation and delithiation and were sealed between polyimide tape and stored in an inert Ar atmosphere. XAS spectra were acquired at sector 12-BM at the Advanced Photon Source at Argonne National Laboratory, IL. All measurements were collected at the Fe K-edge (7.112 keV) in transmission mode using a Si (111) double crystal monochromator with incident and transmission ion chambers filled with 100% N_2. A Fe metal foil reference was used for initial X-ray beam energy calibration and was measured simultaneously with all experimental measurements to ensure proper energy alignment of individual spectra during data analysis.

Each XAS spectrum was aligned, merged, and normalized using Athena.[40,41] The built-in AUTOBK algorithm was used to limit background contributions below R_{bkg} = 1.0 Å. Each Fe_3O_4 electrochemical state was fit utilizing Artemis with theoretical structural models created with FEFF6.[41–43] The series of EXAFS fits were conducted using a combination of inverse-spinel Fe_3O_4,[44] rock-salt FeO[45] and body-centered cubic (bcc) Fe metal[46] crystal structures based on the level of lithiation or delithiation. Each fit was conducted in a k-range of 2–11 $Å^{-1}$ with a Hanning window (dk = 2) in k, k^2 and k^3 k-weights simultaneously. An R-range of 1.0–3.7 Å or 1.0–3.1 Å was typically used to fully encompass the first and second shells of $|\chi(R)|$ (Fourier transform of $\chi(k)$). To account for intrinsic losses from the scattering process that governs XAS, the S_0^2 parameter was determined from fitting a Fe metal reference, and was applied to all fits.

For fully lithiated Fe_3O_4-S and Fe_3O_4-C samples, the contributions of higher order coordination shells were obtained by multiple-scattering EXAFS analysis. Theoretical phases and amplitudes were obtained in self-consistent *ab initio* calculations with FEFF8.5[47] code for bulk iron material. The complex exchange–correlation Hedin–Lundqvist potential and default values of muffin-tin radii as provided within the FEFF8.5 code were employed. Fitting of EXAFS spectra $\chi(k)k^2$ was carried out in R-space in the range from R_{min} = 0.8 Å up to R_{max} = 5.2 Å. Fourier transform was carried out in the k range from 3.0 $Å^{-1}$ up to 12.5 $Å^{-1}$. The bcc structure model was used to generate theoretical amplitudes and phases for all paths included in the fit. We included the nearest single-scattering (SS) and the most important multiple-scattering (MS) paths: linear double and triple scattering paths and double-scattering (DS) paths within the first coordination shell. To reduce the number of independent fitting parameters, all half path lengths R_i of all the (SS and MS) paths used in the fit were constrained to be $R_i = r_i(1 + \varepsilon)$, where r_i is the corresponding value for a model bcc structure and ε is an isotropic lattice expansion/contraction parameter. Coordination numbers for SS contributions were fitted independently, but we constrained MSRD factors for the 2nd Fe–Fe path to be equal to that of the 1st Fe–Fe path, and, similarly, we required MSRD factors of all more distant coordination shells to be equal to the MSRD factor of the 3rd coordination shell. Coordination numbers, distances and disorder parameters in collinear multiple-scattering paths were constrained to be related to those in the corresponding single scattering paths. In addition, to model the oxidation effect, we included in the analysis one Fe–O path, whose coordination number, distance and disorder were also used as fit variables.

Scanning transmission electron microscopy (STEM)

High-angle annular dark-field (HAADF) images were collected on both Fe_3O_4-S and Fe_3O_4-C nanoparticles in fully lithiated and delithiated states using a JEOL ARM 200F microscope equipped with two spherical-aberration correctors and a cold-field-emission electron source. Fe_3O_4-S or Fe_3O_4-C material and acetylene carbon black were mixed in a 1 : 1 ratio in a ball-mixing mill. The mixed powder composites were lithiated and delithiated in coin-type cells with lithium metal anodes and glass fiber separators. Utilizing powder without PVDF binder in the electrode composition facilitated less ambiguity in STEM imaging after electrochemical characterization. Fe_3O_4 particles were removed from electrochemical coin cells, dispersed in dimethyl carbonate and loaded onto a copper grid in an inert Ar atmosphere glovebox. The samples were then sealed within an Ar-filled bag for transferring to the STEM column in order to minimize air exposure.

Results and discussion

Materials characterization

Magnetite, Fe_3O_4 was synthesized using a previously reported coprecipitation approach[17,18] while larger crystallite sized Fe_3O_4 was purchased. Synthesized and commercially obtained Fe_3O_4 materials are denoted Fe_3O_4-S and Fe_3O_4-C, respectively. The Fe_3O_4 samples were characterized by X-ray diffraction and the patterns were indexed to the reported Fe_3O_4 reference pattern (PDF #01-088-0315). Isotropic crystallite sizes were extracted from Rietveld refinement of the data and were determined to be 11.2 nm for Fe_3O_4-S and 39.4 nm for Fe_3O_4-C (Fig. S1, ESI†). The crystallite size of the Fe_3O_4 in the composites was also estimated from the XRD data by applying the Scherrer equation[48] to the FWHM of the (311) peak. Crystallite sizes

estimated using this method were 9 nm and 30 nm for Fe_3O_4-S and Fe_3O_4-C, respectively. From BET surface area measurements, the Fe_3O_4-S and Fe_3O_4-C materials have surface areas of 133 ± 7 and 32 ± 4 $m^2\ g^{-1}$, respectively. Assuming spherical and non-porous particles, these surface areas correspond to average particle diameters of 8.9 ± 0.4 nm for Fe_3O_4-S and 36 ± 4 nm Fe_3O_4-C samples respectively, showing reasonable agreement to the values determined by XRD.

Electrochemistry

Fig. 1 shows representative voltage *vs.* electron equivalent profiles for Fe_3O_4-S and Fe_3O_4-C electrodes. While theoretical lithiation capacity is 924 mA h g^{-1} or 8 electron equivalents, Fe_3O_4-S and Fe_3O_4-C samples have typical lithiation capacities of 1220 mA h g^{-1} and 1130 mA h g^{-1}, respectively. The additional capacity beyond the theoretical value is ascribed primarily to electrolyte decomposition and solid–electrolyte interface (SEI) formation on Fe_3O_4 at low voltage.[49,50] Lithiation of the carbon black conductive additive also contributes ~40 mA h g^{-1} to the overall capacity of the electrode.

Through ~2.5 electron equivalents, the smaller crystallite size Fe_3O_4-S (*ca.* 11 nm) has a higher loaded voltage relative to Fe_3O_4-C (*ca.* 39 nm). This result is consistent with previous reports which attribute reduced polarization to nanosizing, which results in reduced Li^+ diffusion path length.[8,15,17–19,51,52] Polarization, or overpotential, is the deviation of the observed loaded voltage from the thermodynamic open circuit potential.[53] The difference in polarization between the samples is pronounced at lower depths of lithiation, during which lithiation proceeds *via* an insertion process.[3,4] Interestingly, the lithiation plateau at *ca.* 0.83 V associated with the conversion reaction to Li_2O and Fe^0 metal[54] is reached at a lithiation level for Fe_3O_4-C, *ca.* 2.2 electron equivalents, *versus ca.* 3 electron equivalents for Fe_3O_4-S. The data suggests that Li^+ concentration polarization may cause the conversion reaction to occur at lower depth of discharge (DOD) in the larger sized Fe_3O_4.

In situ X-ray diffraction

Fig. 2 and 3 show the *in situ* XRD diffraction patterns for the Fe_3O_4-S and Fe_3O_4-C electrodes respectively. The *in situ* measurements were collected on a laboratory XRD using Cu Kα radiation. The large diffraction peaks observed in both series of XRD diffraction patterns at *ca.* 36°, 52° and 65° correlate to the (110), (200) and (211) Li metal Bragg reflections respectively.[55] At OCV, both the Fe_3O_4-S and Fe_3O_4-C electrodes are in the inverse-spinel $Fd\bar{3}m$ Fe_3O_4 crystal structure with Bragg reflections at *ca.* 30°, 35.5°, 43°, 53.5, 57°, and 63° corresponding to the (220), (311), (400), (422), (511), and (440) lattice planes respectively. All other low intensity, unchanging peaks are attributed to Al foil current collector, Ni current collector tabs, Li metal, separator, and plastic housing directly from the *in situ* experimental set up, as shown by the green trace in Fig. 2 and 3. All unchanging peaks in the XRD patterns align with peaks from the experimental setup. Differences in peak intensity in the green trace representing experimental setup are due to the lack of electrode coating within the cell, particularly for Al foil peaks at 37° and 44.5°.

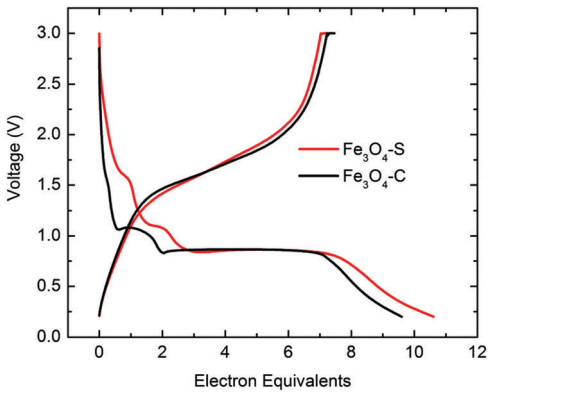

Fig. 1 Representative voltage *vs.* electron equivalent profiles for Fe_3O_4-S and Fe_3O_4-C electrodes lithiated and delithiated at a 0.1C rate in the voltage range 0.2–3.0 V.

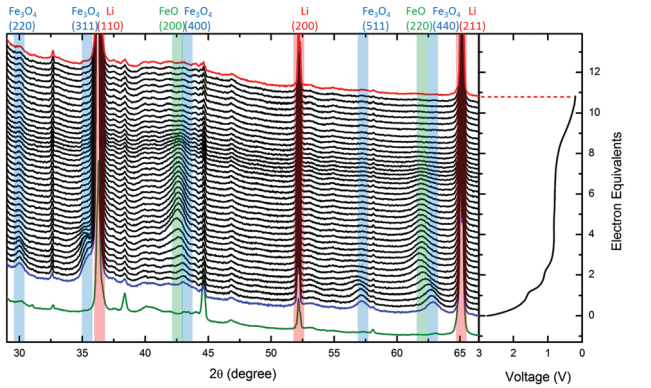

Fig. 2 *In situ* XRD of Fe_3O_4-S during the initial lithiation. XRD scans with blue and red traces show the unlithiated and fully lithiated diffraction patterns. The green trace shows an XRD scan of the experimental setup without the Fe_3O_4 electrode, but including pouch plastic, separator, Al foil, Ni current collector tabs, and Li metal. Peaks attributed to Bragg reflections from Fe_3O_4, Li, and FeO are highlighted in blue, red, and green, respectively.

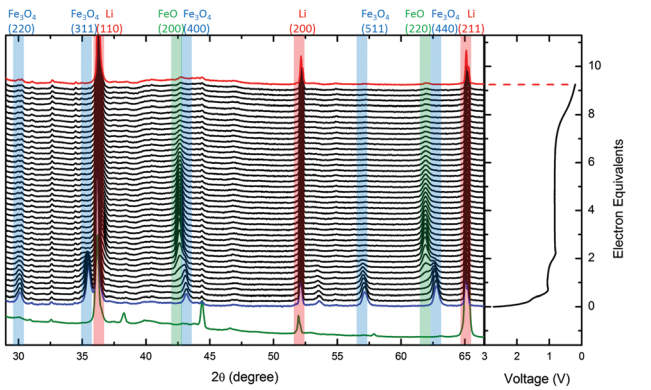

Fig. 3 *In situ* XRD of Fe_3O_4-C during the initial lithiation. XRD scans with blue and red traces show the unlithiated and fully lithiated diffraction patterns. The green trace shows an XRD scan of the experimental setup without the Fe_3O_4 electrode, but including pouch plastic, separator, Al foil, Ni current collector tabs, and Li metal. Peaks attributed to Bragg reflections from Fe_3O_4, Li, and FeO are highlighted in blue, red, and green, respectively.

As both the Fe_3O_4-S and Fe_3O_4-C electrodes begin to lithiate, an expansion of the unit cell is observed from Rietveld analysis as shown in Fig. S5 in the ESI,† with the lattice constant expanding *ca.* 0.7 ± 0.1% for the Fe_3O_4-S and 0.2 ± 0.05% for the Fe_3O_4-C electrode when lithiated up to ~1 e^-. This correlates to an average volumetric expansion of the unit cells of *ca.* 2% and 0.8% respectively, in excellent agreement with previous density functional theory calculations on lithium insertion into the Fe_3O_4 crystal structure.[9] This difference in crystal lattice expansion is attributed to the increased surface area and smaller crystallite size of Fe_3O_4-S compared to the Fe_3O_4-C. The smaller crystallite size allows lithium ions to penetrate the crystal more effectively due to reduced lithium diffusion path length, and has been observed previously in other reports of lithiated Fe_3O_4.[8,15,17–19,51,52] As a result, the crystal lattice undergoes greater expansion in Fe_3O_4-S *versus* Fe_3O_4-C. This hypothesis is supported by the voltage profiles in Fig. 1 which show pronounced polarization at 1 electron equivalent of reduction, indicating that lithium insertion is more kinetically facile into Fe_3O_4-S compared to Fe_3O_4-C.

During the initial lithiation, the expansion and overall retention of the Fe_3O_4 crystal structure is in agreement with previous studies which report that lithium is primarily inserted into vacant sites within the inverse-spinel crystal (likely the 16c site) below *ca.* 1 e^- lithiation,[3,4] along with XRD investigations of similar inverse-spinel crystal structures.[56]

Once both the Fe_3O_4-S and Fe_3O_4-C electrodes are lithiated to *ca.* 2 e^-, conversion to an $Fm\bar{3}m$ FeO-like rock salt structure is observed with Bragg reflections at *ca.* 43° and 62° corresponding to the (200) and (220) lattice planes respectively. The (111) reflection, located at *ca.* 35.7° is also observed as a shoulder that forms on the 35.5° Li metal peak. The lattice constant of this FeO-like phase as determined from Rietveld analysis is 4.2360 ± 0.0005 Å for the Fe_3O_4-C and 4.243 ± 0.003 Å for the Fe_3O_4-S, both of which are smaller than the nominal value of 4.341 Å for standard FeO, suggesting a distorted FeO-like phase is present in each case. When both the Fe_3O_4-S and Fe_3O_4-C electrodes reach the long plateau at *ca.* 0.83 V on the initial lithiation (Fig. 1), the FeO-like diffraction peaks are the most intense during the lithiation, suggesting the maximum amount of crystalline FeO-like phase is present at the onset of the long lithiation plateau, as shown in Fig. 4. The Fe_3O_4-S and Fe_3O_4-C electrodes reach this plateau at different levels of lithiation, ~3 and 2.2 electron equivalents respectively, indicating a difference in the lithiation mechanism with respect to crystallite size during the initial stages of the first lithiation. This FeO-like phase results in similar unit cell parameters as the $Li_xFe_3O_4$ phase previously discussed in the literature in which all Fe atoms transition to vacant octahedral sites during the initial lithiation process.[9] Example unit cells and corresponding XRD patterns of both standard FeO and a $Li_xFe_3O_4$ phase are shown in Fig. S6 (ESI†). As the lithiation progresses, the intensity of the FeO-like diffraction peaks begin to reduce in intensity with no appreciable changes in lattice constant, remaining at 4.237 ± 0.009 Å and 4.232 ± 0.002 Å for Fe_3O_4-S and Fe_3O_4-C respectively at *ca.* 6.5 e^-. In addition, no peak broadening determined from the full-width half maximum is observed (*i.e.* no statistically significant crystallite size changes).

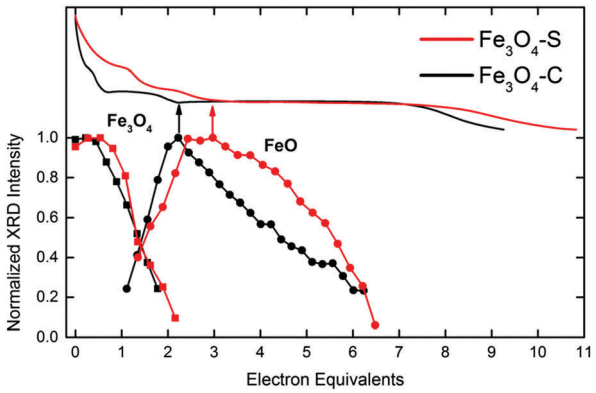

Fig. 4 Relative XRD intensities of Fe_3O_4 and FeO phases in Fe_3O_4-S and Fe_3O_4-C as a function of lithiation. Both phases are normalized to the maximum peak intensity observed during lithiation.

As the FeO-like phase reflections decrease in intensity in the *in situ* XRD pattern, there are no new diffraction peaks that emerge, suggesting that the FeO-like phase is converted to an amorphous or nanocrystalline phase that is unidentifiable through XRD, *i.e.* with no appreciable crystal lattice changes with lithiation of the FeO-like phase, the particles are converted to an amorphous or nanocrystalline phase when fully lithiated. This is fully consistent with the formation of finely divided Fe metal and Li_2O. As both the Fe_3O_4-S and Fe_3O_4-C are delithiated, Fig. S2 (ESI†), there are no significant peaks that evolve in the XRD diffraction patterns even when fully delithiated to 3.0 V. This indicates that the process of lithium removal does not revert the material to a crystalline state, rather it remains in a primarily amorphous or nanocrystalline phase that is not directly detected by XRD. This underlines the necessity of utilizing complementary XAS measurements to accurately characterize the newly formed amorphous/nanocrystalline phases that are difficult to observe using XRD alone.

Recently, a Fickian diffusion based multiscale mathematical model which accounts for mass transport in Fe_3O_4 was developed and validated against experimental discharge and voltage recovery data for Fe_3O_4 electrodes.[25] The study indicated that Li^+ mass transport limitations in the Fe_3O_4 crystals are significantly higher for larger (*ca.* 32 nm) *vs.* smaller (*ca.* 8 nm) crystals. A recent TEM study has also indicated that as a result of the kinetic restrictions through the crystal, conversion reaction to Fe^0 and Li_2O begins before the intercalation reaction is complete, such that lithiated Fe_3O as well as Fe^0 + Li_2O phases exist simultaneously.[54] In the current work, this proposed mechanism can be used to support the observed differences in the lithiation profiles and *in situ* XRD results between the smaller Fe_3O_4-S and larger Fe_3O_4-C crystals. Due to kinetic restrictions, it is reasonable that conversion to Fe^0 + Li_2O will occur on the surface of the crystal before the intercalation process (to form the FeO-like rock salt structure) is complete. Furthermore, the non-homogenous lithiation mechanism is more likely to occur in the Fe_3O_4-C relative to Fe_3O_4-S due to the longer Li^+ diffusion path length in the larger crystal. The lithiation plateau at

ca. 0.83 V associated with the conversion reaction is reached at a lower DOD for Fe_3O_4-C, providing evidence that the conversion reaction does occur earlier in the larger sized material. The depressed lithiation voltage of Fe_3O_4-C relative to Fe_3O_4-S below *ca.* 2 electron equivalents suggests that conversion may be occurring on the surface of the 30 nm crystals at even lower DODs, since conversion reaction occurs at a lower voltage relative to the intercalation step and thus would reduce the observed voltage. Occurrence of the conversion to Fe^0 and Li_2O before FeO phase formation is complete in Fe_3O_4-C also can be used to explain the *in situ* XRD results, which indicates that the maximum intensity of the FeO-like rocksalt phase occurs at a lower electron count for Fe_3O_4-C relative to Fe_3O_4-S. Thus, the electrochemical data and *in situ* XRD results are consistent with a non-homogenous lithiation mechanism which is dependent on Fe_3O_4 crystal size, where increased Li^+ diffusion length in larger crystals results in occurrence of the conversion reaction before the intercalation reaction is complete.

To evaluate further the validity of the non-homogeneous lithiation mechanism, the initial stages of the experiment (up to two electron equivalents of lithiation, x in $Li_xFe_3O_4$) were simulated using a multi-scale model previously developed for the Fe_3O_4 system.[25,57–59] A comparison of the simulated voltage to the experimental data is shown in Fig. 5 which also includes the maximum local concentration predicted by the model at different depths of lithiation. The results indicate that, due to transport limitations, the larger Fe_3O_4 crystallites in the Fe_3O_4-C electrode locally reach higher degrees of lithiation compared to the smaller Fe_3O_4 crystallites in the Fe_3O_4-S electrode. Therefore, the conversion reaction is expected to initiate at earlier depths of lithiation for the Fe_3O_4-C, in excellent agreement with the observed electrochemical characterization.

X-ray absorption near-edge structure (XANES)

Fig. 6 shows the XANES of the Fe_3O_4-S and Fe_3O_4-C during (de)lithiation. During the initial lithiation of the Fe_3O_4-S, as lithium is inserted into the material the edge energy (defined as the maximum of the first derivative of $x\mu(E)$) systematically shifts from 7.127 keV in the unlithiated Fe_3O_4 state to lower energy, indicating an average reduction of the oxidation state of Fe, reaching 7.124 keV by 4 e^- and shifting to a metallic-like edge energy of 7.112 keV when fully lithiated, indicating a primarily Fe^0 oxidation state. Once the material is lithiated past 1 e^-, the subsequent XANES spectra share isobestic points at *ca.* 7.147 and 7.168 keV indicating the material consists of a mixture of two distinct Fe oxidation states past the initial stages of lithium insertion, signifying a direct conversion from an oxidized state to a metallic oxidation state with no intermediate phase.[60,61] The XANES of both the Fe_3O_4-S and Fe_3O_4-C electrodes during the initial lithiation are in agreement with each other, indicating the general lithiation reaction is similar in both crystallite sizes.

As the Fe_3O_4-S electrode is delithiated, XANES spectra at both 2 e^- and 4 e^- appear to be a mixture of metallic and slightly oxidized phases evidenced by the edge positioning. Since spectra at both electron equivalents are nearly identical, it suggests minor fluctuations in the average iron oxidation state in this portion of the charging process. When the Fe_3O_4-S is fully delithiated however, the edge energy reaches 7.124 keV which is slightly lower than the unlithiated edge position of 7.127 keV, revealing the material does not delithiate to form the initial Fe_3O_4 crystal structure. The XANES of the Fe_3O_4-C electrode does not mirror that of the Fe_3O_4-S electrode when delithiated as it did during lithiation. In particular, the white line intensity (at *ca.* 7.131 keV) is significantly reduced in Fe_3O_4-C when fully delithiated compared to that of Fe_3O_4-S. This suggests that these materials are in different local atomic arrangements when fully delithiated, as the XANES region is sensitive to longer-range structures than the EXAFS region due to the energy dependence of the photoelectron mean free path.[62,63]

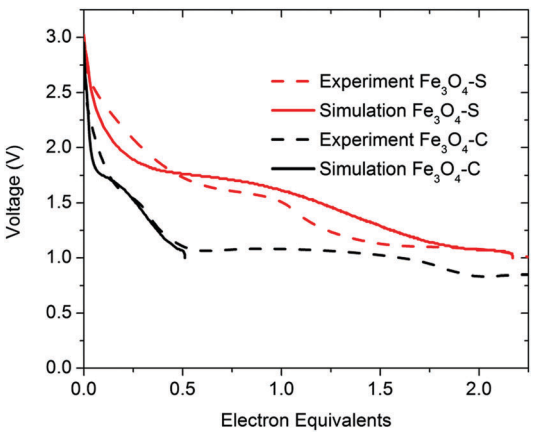

Fig. 5 Comparison of multi-scale model to lithiation data from *in situ* XRD experiment. Numbers on each curve indicate the maximum solid-lithium concentration (x in $Li_xFe_3O_4$) predicted by the model.

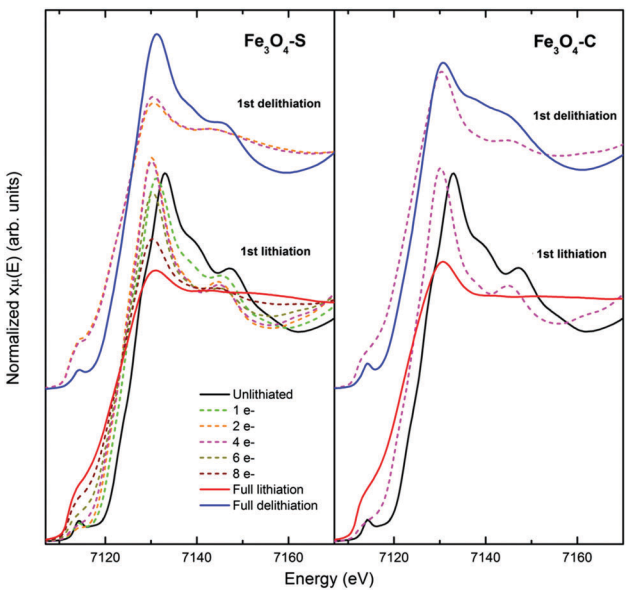

Fig. 6 XANES of Fe_3O_4-S and Fe_3O_4-C electrodes during the lithiation and delithiation.

Extended X-ray absorption fine structure (EXAFS)

The $|\chi(R)|$ (Fourier transform of $\chi(k)$) of all XAS spectra for the lithiation and delithiation of the Fe_3O_4-S are shown in Fig. 7. As was suggested by the XANES and *in situ* XRD results, the initial inverse-spinel Fe_3O_4 structure is maintained through 1 e^- lithiation with no substantial changes in $|\chi(R)|$. However, once the material is lithiated to 2 e^-, there is a dramatic change in crystal structure, converting from Fe_3O_4 to an FeO-like phase as evidenced by a shift in Fe–O peak position at *ca.* 1.4 Å as well as a change in the second shell peak centered at *ca.* 2.5 Å (the distances displayed in Fig. 7 are not corrected for phase shifts from the scattering process that governs XAS measurements and are *ca.* 0.3 Å shorter than the phase-corrected interatomic distances determined from modeling). The observation of this FeO-like phase in $|\chi(R)|$ at 2 e^- is in excellent agreement with the *in situ* XRD results (Fig. 2). As the material continues to lithiate, metallic Fe is first observed in the EXAFS spectra beginning at 6 e^-. Once fully lithiated, a strong metallic Fe peak emerges at *ca.* 2.3 Å in Fig. 7. This corresponds well to the XANES analysis that suggested a primarily metallic oxidation state when fully lithiated (Fig. 6).

As the Fe_3O_4-S electrode is delithiated, the local atomic environment at 2 e^- and 4 e^- are very similar. Visual inspection of $|\chi(R)|$ suggest the electrode is a mixture of oxidized and metallic Fe at these stages of delithiation. However, once the material is fully delithiated at 3.0 V, the peak positions suggest the formation of a FeO-like structure, similar to the FeO-like phase formed during the initial lithiation at 2 e^- and 4 e^-. Since there is no observation of the reformation of a FeO-like phase from the *in situ* XRD measurements, this suggests this reformation is highly disordered or nanocrystalline.

The EXAFS spectra were fit using theoretical structural models to determine the interatomic distance between Fe and neighboring O or Fe atoms along with the corresponding relative amplitude of each phase (defined as the scaled number of near neighbors in each phase, with a bulk crystallite having the relative amplitude of 1), shown in Fig. 8. Contributions from neighboring O (green, Fe–O from Fe_3O_4 and FeO-like phases), Fe from Fe_3O_4 (black, Fe–Fe), Fe from the FeO crystal structures (red, Fe–Fe) and Fe from metallic Fe (blue, Fe–Fe metal) are presented. For Fe–Fe paths from Fe_3O_4, octahedral paths are denoted as filled square icons and tetrahedral paths are denoted as open square icons. The fitted relative amplitudes of all Fe_3O_4 Fe–Fe paths were equivalent, thus the for the relative amplitude portion of the figure, only one set of points is visible. Full detailed fitting parameters results are presented in the ESI.† The reported relative amplitude of each phase is lower than the expected values due to the sufficiently small particle sizes. With a larger surface-to-bulk ratio, the average number of observed neighboring atoms is intrinsically lower than the bulk values, resulting in a lower observed amplitude/average number of neighboring atoms determined from modeling. When two distinct phases are present, the relative amplitudes can provide an estimate of the relative ratio of phases present in the material. When a single phase is present, the reduced amplitude can be indicative of the average particle size/morphology.[64–69]

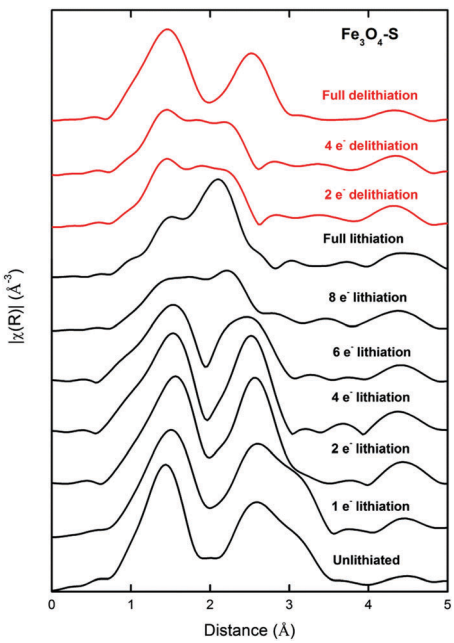

Fig. 7 k^2 weighted $|\chi(R)|$ of the 1st lithiation and delithiation of Fe_3O_4-S. Lithiated states are indicated as black lines while the delithiated states are in red lines. Distances indicated are not corrected for phase shifts, causing the peak positions to be *ca.* 0.3 Å shorter than the phase-corrected interatomic distances determined from modeling.

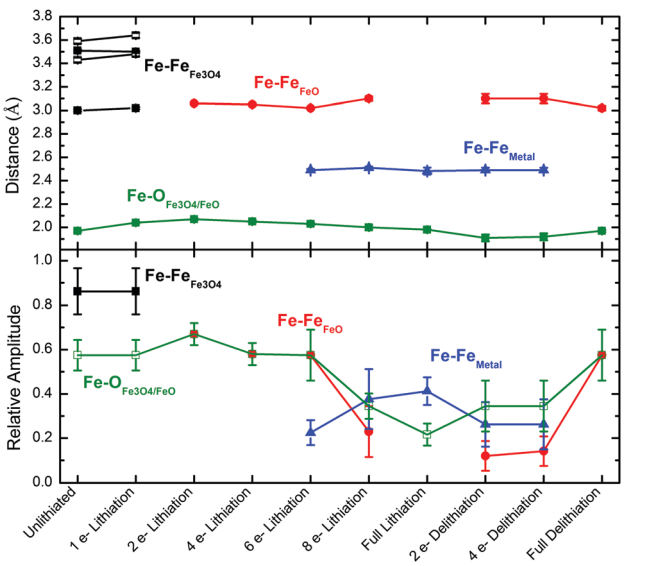

Fig. 8 Interatomic distance and relative amplitudes of Fe_3O_4, FeO and Fe metal phases determined from EXAFS modeling results for Fe_3O_4-S during the initial lithiation and delithiation. Contributions from neighboring O (green, Fe–O from Fe_3O_4 and FeO-like phases), Fe from Fe_3O_4 (black, Fe–Fe), Fe from the FeO crystal structures (red, Fe–Fe) and Fe from metallic Fe (blue, Fe–Fe metal) are presented. For Fe–Fe paths from Fe_3O_4, octahedral paths are denoted as filled square icons and tetrahedral paths are denoted as open square icons. The fitted relative amplitudes of all Fe_3O_4 Fe–Fe paths were equivalent, thus the for the relative amplitude portion of the figure, only one set of points is visible. All results are presented in full in the ESI.† In the upper panel, error bars are included but are smaller than the symbols for the reported interatomic distances.

As was observed in the Rietveld analysis of the *in situ* XRD spectra, an expansion in interatomic distances is observed between the unlithiated and 1 e^- lithiated state, particularly between the tetrahedrally coordinated Fe (located at 8a sites) and the octahedrally coordinated Fe (16d sites) expanding from 3.59 ± 0.02 Å in the unlithiated state to 3.64 ± 0.02 Å at 1 e^- lithiation (*ca.* 1.4% expansion in interatomic distance that correlates well to the calculated volume expansion of *ca.* 2% from *in situ* XRD Rietveld analysis). When lithiated to 2 e^- the EXAFS spectrum could no longer be modeled using the inverse-spinel Fe_3O_4 crystal structure, rather a FeO crystal model was adopted. From this structure, two Fe–O contributions and one Fe–Fe contribution was used. Fitted distances of 2.07 ± 0.01 Å, and 3.06 ± 0.01 Å were found for nearest neighbor Fe–O and Fe–Fe paths respectively, which correspond well to the expected contraction of the standard FeO structure from the reduced lattice parameters determined from *in situ* XRD measurements (Fe–O and Fe–Fe interatomic distances of 2.17 Å and 3.07 Å respectively). An additional long Fe–O path associated with the FeO structure at 3.79 ± 0.05 Å was needed to produce a fit with *R*-factor < 2.0. For samples further lithiated to 4, 6, and 8 electron equivalents, the path at *ca.* 3.79 Å was no longer necessary to model the data; however, an Fe–O path at *ca.* 2.7 Å was needed to produce an acceptable fit due to residual signal in the second coordination shell. The extra Fe–O path is not associated with the FeO crystal structure and has previously been used in conjunction with the FeO phase to model discharging Fe_3O_4 electrodes.[70] The path is postulated to arise from the formation of the Li_2O phase during discharge, where the contribution of Li_2O is significant due to the large percentage of surface iron atoms on the surface of the discharging FeO particle.

Once the Fe_3O_4-S electrode is lithiated to 6 e^-, a mixture of Fe metal and FeO is first observed. The Fe metal that forms has a Fe–Fe interatomic distance of 2.49 ± 0.01 Å (crystalline bcc Fe metal has a Fe–Fe distance of 2.48 Å).[46] Continued lithiation results in the disappearance of the FeO-like structure past 8 e^-, leaving only metallic Fe with a relative amplitude of 0.46 ± 0.09 with an interatomic distance of 2.46 ± 0.02 Å in the fully lithiated state. As the Fe_3O_4-S electrode is delithiated the FeO-like structure begins to form. Neighboring Fe atoms reemerge at an interatomic distance of 3.10 ± 0.04 Å, similar to the Fe–Fe distance observed during initial lithiation (3.10 ± 0.02 Å at 8 e^- lithiation) for the FeO-like phase. The local atomic structure at both 2 and 4 e^- during lithium removal are remarkably similar, with all interatomic distances and relative amplitudes of the FeO-like and Fe metal phases within estimated standard deviations of each other. Once the material is fully delithiated, Fe metal is no longer observed in the EXAFS spectrum resulting in only a FeO-like structure. The delithiated FeO-like structure has a shorter Fe–O distance (1.97 ± 0.01 Å) compared with the FeO structure used to model the lithiation process (2.05 ± 0.01 Å at 4 electron equivalents of lithiation). The contraction of the Fe–O distance suggests that the delithiated phase is less crystalline and more disordered than the structure during initial delithiation. A higher Debye–Waller factor associated with the Fe–O bond for the delithiated phase (0.011 ± 0.002 for delithiated phase *vs.* 0.007 ± 0.002 for 4 electron equivalents of lithiation) also indicates a greater degree of disorder for the delithiated phase. Furthermore, the XRD result supports the hypothesis that the reformed phase is nanocrystalline, as it is not detected by diffraction.

The Fe_3O_4-C electrode follows a similar trend as the Fe_3O_4-S electrode during the 1st lithiation, as shown in Fig. 9, which includes k^2 weighted $|\chi(R)|$ comparison of the Fe_3O_4-S and Fe_3O_4-C in Fig. 9a and the relative amplitude of Fe_3O_4, FeO, and Fe metal phases for both electrode types shown in Fig. 9b. From the initial Fe_3O_4 crystal structure, the material converts to a FeO-like phase by 4 e^-, analogous to the discharge of Fe_3O_4-S. However, unlike the Fe_3O_4-S electrode, there is also an indication of Fe metal at this state of lithiation as shown by a shoulder forming in $|\chi(R)|$ at *ca.* 2.2 Å (Fig. 9a) that is not observed in the Fe_3O_4-S electrode. The Fe metal contribution is reflected in the EXAFS fit at 4 e^- for Fe_3O_4-C (Fig. 9b), with relative amplitude of 0.25. In agreement with the first cycle lithiation profile, *in situ* XRD results, and multi-scale simulations, the data suggests that conversion to Fe metal occurs in the larger Fe_3O_4-C crystallites at a lower DOD relative to the smaller Fe_3O_4-S crystallites. This is

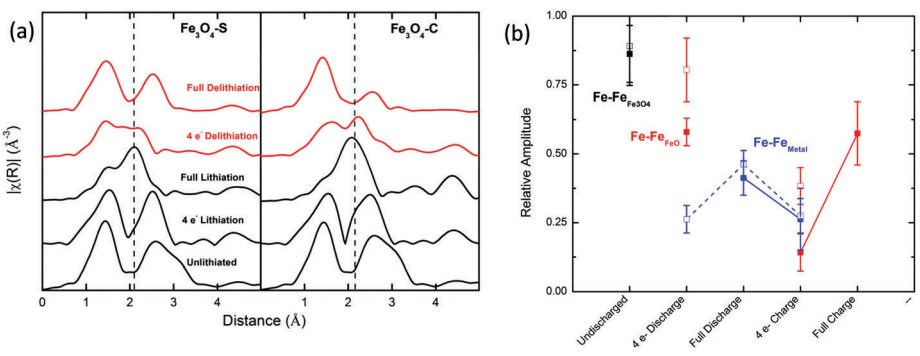

Fig. 9 (a) k^2 weighted $|\chi(R)|$ comparison of the Fe_3O_4-S and Fe_3O_4-C. The initial lithiation is shown in black, and initial delithiation in red. (b) Relative amplitude of Fe_3O_4 (black), FeO-like (red) and Fe metal (blue) phases determined from EXAFS fitting results for both Fe_3O_4-S and Fe_3O_4-C nanoparticles during various (de)lithiation states. The solid symbols connected by solid lines are the Fe_3O_4-S results, while the open symbols connected by dashed lines are the Fe_3O_4-C results.

further evidence that the initial lithiation process in Fe_3O_4 happens *via* a non-homogenous lithiation mechanism which is dependent on Fe_3O_4 crystal size. Because of kinetic restrictions associated with longer Li^+ diffusion length in the larger Fe_3O_4 crystallites, in order to accommodate the flux of electrons the conversion reaction must occur concurrent to the insertion reaction.

Upon full lithiation in the Fe_3O_4-C, the $|\chi(R)|$ suggest a primarily metallic local atomic environment around Fe, similar to the fully lithiated Fe_3O_4-S electrode. Conversely, when the Fe_3O_4-C is fully delithiated, it is clear that it does not return to the same local crystal structure as the Fe_3O_4-S as seen from the relative peak heights at ~1.4 Å and 2.7 Å in Fig. 9 at both 4 e^- and fully delithiated electrochemical states. During delithiation, the Fe_3O_4-S fully re-converted to a FeO-like structure, similar to that observed during the initial lithiation, while the fully delithiated Fe_3O_4-C does not have a discernable crystal structure. Only neighboring oxygen atoms (with no statistically significant neighboring Fe contributions) could be determined from the EXAFS spectrum. The lack of Fe–Fe neighboring atoms and differences in interatomic distances compared to the Fe_3O_4-S suggest that the Fe_3O_4-C delithiations to a primarily amorphous or nanocrystalline iron oxide state, while the delithiated Fe_3O_4-S exhibits some degree of crystallinity of a FeO-like rock salt structure. Furthermore, additional Fe–O paths in the second coordination shell were needed to produce good fits for the delithiated samples, with Fe_3O_4-S and Fe_3O_4-C having Fe–O interatomic distances of 2.59 ± 0.05 Å and 3.04 ± 0.02 Å respectively. These second shell Fe–O oxygen paths are hypothesized to be due to the highly disordered state nature of the re-oxidized iron oxide. Similar second-shell Fe–O paths have been observed in the charged state of other spinel-type conversion materials $CuFe_2O_4$ and $ZnFe_2O_4$ *via* EXAFS.[71,72]

EXAFS analysis of distant coordination shells in fully lithiated samples

In order to further investigate the differences between the Fe metal phase formed in the fully lithiated state between Fe_3O_4-S and Fe_3O_4-C crystallites, for these 2 samples the contributions of higher order coordination shells were determined by multiple-scattering EXAFS analysis in the *R*-space range from R_{min} = 0.8 Å up to R_{max} = 5.2 Å. Details of the fitting procedures are provided in the Experimental section. The data were compared with Fe K-edge EXAFS data for bulk reference compounds, as well as for previously published Fe nanoparticle EXAFS data.[73] In this previous work, high temperature H_2 treatment of an iron based oxygen reduction catalyst size resulted in Fe NPs that were estimated to be ~1.0–1.5 nm, based on fitted coordination numbers for nearest neighbor Fe–Fe shells and assuming bcc-type structure and cubic shape.[73] EXAFS fitting results are shown in Fig. 10 and structural parameters obtained from the fits are shown in Table 1.

As shown in Table 1, the Fe–Fe and Fe–O distances for Fe NPs, Fe_3O_4-S and Fe_3O_4-C agree within error bars. The obtained Fe–Fe distances for Fe_3O_4-S and Fe_3O_4-C also agree well with the Fe–Fe distances in bulk Fe metal. Also, the Fe–Fe coordination numbers are significantly smaller than could be expected for NPs

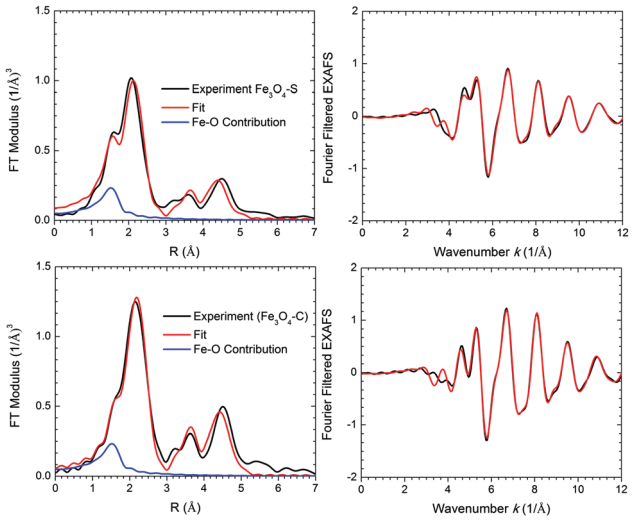

Fig. 10 EXAFS fitting results of Fe metal nanoparticles and fully lithiated Fe_3O_4-S and Fe_3O_4-C electrodes.

of sizes *ca.* 11 and 39 nm. This indicates that the sample is significantly non-homogeneous, with a large contribution of ultra-small (<nm) Fe clusters. Furthermore, it is notable the bond length disorder factor is consistently higher for lithiated Fe_3O_4-S particles compared to lithiated Fe_3O_4-C particles.

The contribution of oxide phase is relatively small, as evidenced by small average Fe–O coordination number. We can estimate the fractions of oxide and metallic phase using the obtained value for Fe–O coordination number. By definition this coordination number should be equal to:

$$N_O = \frac{n_{Fe-O}}{n_{Fe}} = \frac{x n_{Fe} \times 6}{n_{Fe}} = 6x,$$

where n_{Fe} total number of Fe atoms in the sample, n_{Fe-O} total number of Fe–O bonds, x is molar concentration of oxide phase, and it is assumed that each Fe atom in oxide phase is surrounded by 6 oxygen atoms. Thus, the concentrations of

Table 1 Structure parameters (coordination numbers *N*, interatomic distances *R*, and disorder factors σ^2), obtained in fitting of experimental EXAFS data for Fe nanoparticles

	R_O (Å)	R_{Fe_1} (Å)	R_{Fe_2} (Å)	R_{Fe_3} (Å)	R_{Fe_4} (Å)	R_{Fe_5} (Å)
Iron foil	—	2.47(1)	2.85(1)	4.03(1)	4.73(1)	4.94(1)
Fe NPs[73]	1.981(2)	2.481(3)	2.865(3)	4.053(5)	4.753(5)	4.964(6)
Fe_3O_4-S	1.981(3)	2.481(4)	2.865(5)	4.053(7)	4.753(8)	4.964(9)
Fe_3O_4-C	1.981(2)	2.482(3)	2.866(3)	4.054(5)	4.755(6)	4.966(6)
	σ_O^2 (Å^2)	$\sigma_{Fe_1}^2$ (Å^2)	$\sigma_{Fe_2}^2$ (Å^2)	$\sigma_{Fe_3}^2$ (Å^2)	$\sigma_{Fe_4}^2$ (Å^2)	$\sigma_{Fe_5}^2$ (Å^2)
Iron foil	—	0.004(1)	0.005(1)	0.007(2)	0.010(1)	0.004(1)
Fe NPs[73]	0.01(1)	0.005(1)	0.005(1)	0.009(3)	0.009(3)	0.009(3)
Fe_3O_4-S	0.006(3)	0.007(1)	0.007(1)	0.014(5)	0.014(5)	0.014(5)
Fe_3O_4-C	0.006(14)	0.006(1)	0.006(1)	0.012(3)	0.012(3)	0.012(3)
	N_O	N_{Fe_1}	N_{Fe_2}	N_{Fe_3}	N_{Fe_4}	N_{Fe_5}
Iron foil	—	8	6	12	24	8
Fe NPs[73]	0.7(4)	5.8(7)	2.3(5)	7(3)	15(4)	1(1)
Fe_3O_4-S	1.3(3)	3.3(5)	0.5(3)	4(2)	6(4)	2(1)
Fe_3O_4-C	1.3(3)	3.7(4)	1.3(3)	5(2)	8(3)	2(1)

oxide phase are about 11% in sample from ref. 73 and about 22% in both Fe_3O_4-S and Fe_3O_4-C nanoparticles.

The coordination for Fe–O atoms, as measured by EXAFS, is reduced $1/x$ times due to presence of other phase in the sample. Similarly, the true coordination numbers for Fe–Fe bonds are reduced $1/(1-x)$ times with respect to those given in Table 1.[74] The corrected values of coordination numbers for the first five coordination shells are summarized in Table 2.

The coordination numbers for 2nd and 5th coordination shells correlate strongly with other fitting parameters. Coordination numbers for the 1st, 3rd and 4th coordination shells are less sensitive to the details of used fitting scheme and are therefore used to estimate approximately the Fe nanoparticle sizes. Fig. 11 displays calculated behaviors of the coordination numbers for 1st, 3rd and 4th shell as a function of nanoparticle size, corresponding to cubic shape and bcc structure of the model particles.[75] The corresponding best fit values, together with their error bars, are shown as well. The intercepts of the experimental values and model curves define the region of sizes where experiment and model are generally consistent.[75] For the lithiated Fe_3O_4-S sample, the regions corresponding to different coordination shells overlap in the 0.5–1.0 nm range, which indicates that the Fe particles are, on the average, approximately 0.5–1.0 nm in size. Similarly, particles in the lithiated Fe_3O_4-C sample are estimated to be, on the average, approximately 0.7–1.0 nm in size.

The EXAFS analysis of the fully lithiated Fe_3O_4-S and Fe_3O_4-C particles and associated modeling of the apparent sizes of the reduced Fe nanoparticles formed indicate that the main difference between the fully lithiated Fe_3O_4-S and Fe_3O_4-C particles is the larger bond length disorder in the Fe_3O_4-S sample. This greater disorder, together with the slightly smaller size of the Fe domains, may allow the Fe_3O_4-S material to more effectively delithiate to a uniform FeO-like structure in the fully delithiated state compared to the Fe_3O_4-C sample.

Scanning transmission electron microscopy (STEM)

Fig. 12 shows the HAADF images recorded from the two samples containing Fe_3O_4-S and Fe_3O_4-C nanoparticles that have been fully lithiated and fully delithiated. Metallic Fe nanograins were observed in both samples when fully lithiated (Fig. 12a–d). The Fe metal that is formed in both the lithiated Fe_3O_4-S and lithiated Fe_3O_4-C appear to be irregularly shaped nanograins and not a uniform morphology. These results correspond well with the EXAFS analyses, which indicate the formation of highly nanocrystalline Fe metal upon lithiation.

The HAADF images from the fully delithiated samples show a considerable difference in the microstructure of the formed FeO-like phase. In the Fe_3O_4-S sample homogeneous FeO-like crystallites were formed with uniform microstructure (Fig. 12e). This matches well with the EXAFS modeling results, which reveal a FeO-like structure similar to that observed in the initial lithiation (Fig. 8). However, the FeO-like phase that is formed in the Fe_3O_4-C electrode exhibits a high degree of disorder, with clear misalignment of a *ca.* 11° rotation between neighboring FeO-like sub-grains (Fig. 12f). This observation appears to be consistent with EXAFS modeling results showing considerable disorder in the delithiated FeO-like phase in the Fe_3O_4-C electrode compared to the delithiated state of the Fe_3O_4-S electrode (Fig. 9).

Table 2 Coordination numbers N for Fe–O and Fe–Fe bonds in Fe NPs, corrected for presence of oxide phase

	N_O	N_{Fe_1}	N_{Fe_2}	N_{Fe_3}	N_{Fe_4}	N_{Fe_5}
Iron foil	—	8	6	12	24	8
Fe NPs[73]	6	6.6(8)	2.6(6)	8(3)	17(5)	1(1)
Fe_3O_4-S	6	4.2(9)	0.6(4)	5(3)	8(5)	3(1)
Fe_3O_4-C	6	4.7(5)	1.7(4)	6(3)	10(4)	3(1)

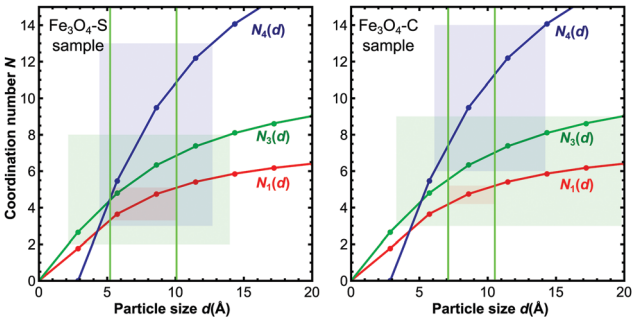

Fig. 11 Red, green and blue dots and solid lines show calculated dependencies of coordination numbers $N_1(d)$, $N_3(d)$ and $N_4(d)$ on particle size d for cubic particles with bcc-type Fe structure. Vertical positions and heights of filled rectangles correspond to the best fit values for coordination numbers N_1 (red), N_3 (green) and N_4 (blue) and their uncertainties for Fe NPs material. The area between two vertical green lines shows the range of particle sizes, consistent with the values for N_1, N_3 and N_4, obtained from fit.

Modeling of Fe nanograin sizes as a function of shape

Motivated by the EXAFS analysis and TEM results, we considered different structural models of the Fe clusters generated from the

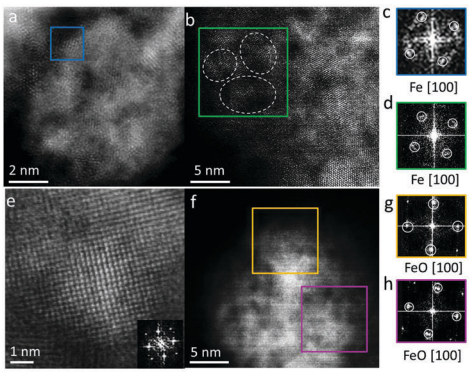

Fig. 12 Microstructures of Fe_3O_4-S and Fe_3O_4-C nanoparticles after full lithiation and delithiation. (a and b) HAADF images showing Fe nanograins in the lithiated Fe_3O_4-S and Fe_3O_4-C nanoparticles, respectively. Several Fe nanograins were formed within the local area marked by white circles in (b). (c and d) Fast Fourier Transform (FFT) patterns obtained from the local regions in (a) and (b), indicating the presence of Fe phase. (e and f) HAADF images showing the formation FeO-like structure of the delithiated Fe_3O_4-S and Fe_3O_4-C nanoparticles, respectively. The inset FFT pattern in (e) indicates that the nanoparticle was projected along the [100] zone axis. The rotation between FFT patterns in (g) and (h), which were obtained from two different FeO-like sub-grains in the yellow and purple boxes in (f), shows the misorientation of about 11° rotation between these two sub-grains.

bulk bcc structure. In addition to the cubic shape assumed in the previous EXAFS analysis (Fig. 11), we also examined spherical and square cylindrical shapes. The latter is included to better capture the structural characteristics of the irregularly shaped Fe nanograins that are only a few atomic layers thick, and the cylindrical axis is taken to be along the [100] direction as suggested by TEM (Fig. 12). The height of the cylinder is defined in unit of the bulk lattice constant, $h = m{\cdot}a_0$, with $a_0 = 2.87$ Å, and we only consider cases with h equal to or smaller than lateral size of the cluster. Fig. 13 plots the average coordination number of 1st coordination shell (N_1) as a function of cluster size for spherical, cubic and square cylindrical shapes. For the spherical case, the approximate form derived by Calvin *et al.*[66] was adopted, with $N_1 = [1 - 3/4(d_0/R) + 1/16(d_0/R)^3]N_{\text{bulk}}$, where $N_{\text{bulk}} = 8$ for bcc Fe and d_0 is taken to be the bulk Fe–Fe distance $d_0 = \sqrt{3}a_0/2$. When the size of the cluster becomes larger than 1 nm, $(N_{\text{bulk}} - N_1)$ is dominated by the $1/D$ behavior with $D = 2R$. A similar trend is found for the cubic case, for which N_1 takes an exact analytical form of $N_1 = 16n^3/(1 + 3n + 3n^2 + 2n^3)$, where $D = na_0$ is the cluster size (edge length) of the cubic cluster. As the thickness of a cubic cluster decreases, *i.e.* changing into a square cylindrical shape, contributions to N_1 from low-coordinated surface atoms becomes more important, leading to an overall reduction of N_1, as clearly demonstrated in Fig. 13 for $m = 1$–4. Here $m = 1$ correspond to a trilayer nanofilm with height equal to a_0.

If we consider square cylindrical shapes in the EXAFS analysis, the upper limit of the fitted Fe cluster size may be further extended. For example, for the Fe_3O_4-C nanoparticles ($N_1 = 4.7(5)$ from Table 2), the fitted Fe cluster size by assuming a cubic shape (filled red rectangle in Fig. 13) is increased by nearly 0.5 nm by including square cylindrical shape with $m = 2$ (open green rectangle). If $m = 1$ is also considered, the fitted size range will be even larger. Of course, an accurate estimate of the Fe cluster size requires taking into considerations all other constraints, such as those provided by higher neighbor coordination numbers. Based on these calculations, the low values of N_1 of the Fe_3O_4-S and Fe_3O_4-C nanoparticles are likely caused by both the size and shape of the Fe nanograins formed when fully lithiated. Since the nanocrystalline nature of the Fe nanograins may be critical for reversibility back to the delithiated state, Fe nanograin dimensions will be further considered as a part of future studies on Fe_3O_4 electrodes.

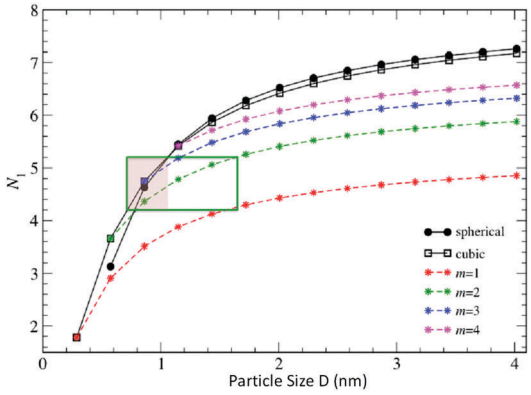

Fig. 13 Average coordination number for the 1st coordination shell (N_1) of cubic, spherical and square cylindrical bcc Fe clusters of different sizes. The filled red and open green rectangles correspond to fitting N_1 of the Fe_3O_4-C nanoparticles to cubic shape and square cylindrical shape ($m = 2$) respectively.

(De)lithiation mechanism

The combination of *in situ* XRD, continuum-level simulations, *ex situ* XAS and STEM images has permitted a comprehensive study of the structural differences in the (de)lithiation mechanisms of Fe_3O_4-S (*ca.* 11 nm Fe_3O_4) and Fe_3O_4-C (*ca.* 39 nm Fe_3O_4) nanoparticles. Regardless of crystallite size of Fe_3O_4, the first lithiation follows a similar mechanism. During initial lithiation (below $\sim$1 e^-), lithium is inserted into the vacant sites within the Fe_3O_4 inverse-spinel crystal structure, resulting in the expansion of the crystal structure but an overall retention of the crystal symmetry and occupancy as determined from Rietveld refinement of the *in situ* XRD spectra. As the material lithiation continues, a phase change occurs, converting Fe_3O_4 to a FeO-like rock salt structure at $\sim$2 e^-.

Further lithiation initiates another phase change from the FeO-like structure to an amorphous or nanocrystalline metallic Fe^0 accompanied by Li_2O formation. The metallic Fe^0 that is formed was not directly observable by XRD measurements, but XANES and EXAFS analysis clearly show an average reduction in the oxidation state of the Fe centers towards a Fe^0 oxidation state. Notably, the XANES of the Fe_3O_4-S exhibits several isobestic points from the FeO-like phase at 2 e^- until it is fully lithiated to primarily metallic Fe^0, suggesting that only two distinct Fe oxidation states are present within the sample (*i.e.* the FeO-like phase and metallic Fe). For this observation to hold true a direct conversion from the FeO-like phase to metallic Fe must occur with no intermediate phase. From the *in situ* XRD spectra and subsequent Rietveld refinement, there is no significant change in the unit cell parameters during this conversion, rather a reduction in overall intensity of the observed Bragg reflections in both the Fe_3O_4-S and Fe_3O_4-C electrodes of the FeO-like phase. Moreover, the EXAFS modeling results indicate that both the Fe_3O_4-S and Fe_3O_4-C electrodes exhibit no appreciable deviation in the interatomic distances related to the FeO-like phase until nearly full conversion to Fe metal at 8 e^-. As noted, a reduction in the relative amplitude of the FeO-like phase is observed with further lithiation. This suggests the individual FeO-like crystallites are directly converted to Fe metal and Li_2O, *i.e.* any structural changes that may occur during this transition are small compared to the bulk of the electrode which remains unaltered.

The conversion to Fe metal does not occur homogenously and is dependent on the Fe_3O_4 crystallite size. *In situ* XRD results indicate that the maximum intensity of the FeO-like rocksalt phase occurs at a lower electron count for Fe_3O_4-C relative to Fe_3O_4-S, while at the same time the first cycle lithiation curves and continuum-level simulations suggest that Fe conversion occurs earlier for Fe_3O_4-C. Furthermore, Fe metal is observed at lower DOD for the Fe_3O_4-C *via* EXAFS analysis. These observations all suggest that kinetic restrictions of Li^+ diffusion in the larger

sized Fe_3O_4-C crystals necessitate initiation of the conversion reaction before the process of lithium insertion into Fe_3O_4 inverse-spinel crystal structure is complete. This type of non-uniform lithiation mechanism underscores the importance of lithium ion diffusion kinetics in nanosized Fe_3O_4.

Multiple-scattering EXAFS analysis of Fe_3O_4-S and Fe_3O_4-C samples in the fully lithiated state indicates that the lithiated samples are non-homogeneous, with a large contribution of ultra-small (<nm) Fe clusters. Modeling of the sizes of these clusters using coordination numbers of higher order coordination shells resulted in estimated Fe particle sizes of approximately 0.5–1.0 nm for the Fe_3O_4-S sample and approximately 0.7–1.0 nm for the Fe_3O_4-C sample. Furthermore, the analysis also indicated that the Fe formed in Fe_3O_4-S particles has greater bond length disorder compared to Fe formed in Fe_3O_4-C particles.

The Fe_3O_4-S is able to return to a cohesive FeO-like phase that is similar to what is formed during the first lithiation as evidenced again by EXAFS results and HAADF images. The Fe_3O_4-C, however, does not reform to any recognizable iron oxide structure through EXAFS analysis. Rather it becomes a highly disordered FeO-like phase as shown by the microstructure in the HAADF images, with FeO-like nanocrystal grains on the order of several nanometers significantly misaligned with neighboring nanograins, creating a highly localized FeO-like phase. We hypothesize that the comparably greater disorder and the smaller size of the Fe domains in the fully lithiated Fe_3O_4-S particles, as determined by multiple-scattering EXAFS analysis, may allow for the Fe_3O_4-S material to more effectively delithiate to a FeO like structure in the fully delithiated state compared to the Fe_3O_4-S sample. The smaller, more disordered Fe domains facilitate reaction with Li_2O domains enabling conversion to a homogeneous FeO-like structure upon Li removal. In contrast, the efficiency of the oxidation reaction with Li_2O is reduced in the larger, more ordered domains found in lithiated Fe_3O_4-C sample, resulting in fractured and misaligned nanograins of the FeO-like phase.

Conclusions

In summary, this work utilized complementary *in situ* XRD, continuum-level simulations, *ex situ* XAS and STEM measurements to determine the crystal and local atomic structural changes that occur during electrochemical cycling of Fe_3O_4-S (*ca.* 11 nm Fe_3O_4) and Fe_3O_4-C (*ca.* 39 nm Fe_3O_4). Tracking the crystalline and nanocrystalline phases during the first lithiation provided evidence of a non-uniform, crystal size dependent lithiation mechanism, where increased Li^+ diffusion length in larger crystals results in conversion to Fe^0 metal while insertion of Li^+ into spinel-Fe_3O_4 is still occurring. Furthermore, the data suggest that the disorder inherent to the Fe metal domains formed when either material is fully lithiated impact the homogeneity of the FeO phase formed during the subsequent delithiation. Lithiation of Fe_3O_4-S results in smaller, more disordered Fe domains compared to Fe_3O_4-C. These disordered domains more efficiently react with Li_2O domains to reconvert to a homogeneous FeO-like structure during Li removal, while more ordered Fe domains result in fractured and misaligned nanograins of a FeO-like phase.

Acknowledgements

This work was supported as part of the Center for Mesoscale Transport Properties, an Energy Frontier Research Center supported by the U.S. Department of Energy (DOE), Office of Science, Basic Energy Sciences, under award #DE-SC0012673. XAS measurements used the resources of the Advanced Photon Source, a DOE, Office of Science User Facility operated for the DOE Office of Science by Argonne National Laboratory under Contract No. DE-AC02-06CH11357. The computing associated with Fig. 5 was performed on the Yeti Shared HPC Cluster at Columbia University, which includes support from Empire State Development's Division of Science, Technology, and Innovation under contract number C090171. A. I. F. and J. T. acknowledge support from the US National Science Foundation Grant CHE-1534184 for the multiple-scattering EXAFS data analysis in Fig. 10 and 11 and Tables 1 and 2.

Notes and references

1 A. M. Bruck, C. A. Cama, C. N. Gannett, A. C. Marschilok, E. S. Takeuchi and K. J. Takeuchi, *Inorg. Chem. Front.*, 2016, **3**, 26–40.
2 M. E. Fleet, *J. Solid State Chem.*, 1986, **62**, 75–82.
3 M. M. Thackeray, W. I. F. David and J. B. Goodenough, *Mater. Res. Bull.*, 1982, **17**, 785–793.
4 J. Fontcuberta, J. Rodriguez, M. Pernet, G. Longworth and J. B. Goodenough, *J. Appl. Phys.*, 1986, **59**, 1918–1926.
5 M. Thackeray, L. De Picciotto, A. De Kock, P. Johnson, V. Nicholas and K. Adendorff, *J. Power Sources*, 1987, **21**, 1–8.
6 M. Islam and C. Catlow, *J. Solid State Chem.*, 1988, **77**, 180–189.
7 T. Yamada, K. Morita, K. Kume, H. Yoshikawa and K. Awaga, *J. Mater. Chem. C*, 2014, **2**, 5183–5188.
8 M. C. Menard, K. J. Takeuchi, A. C. Marschilok and E. S. Takeuchi, *Phys. Chem. Chem. Phys.*, 2013, **15**, 18539–18548.
9 W. Zhang, D. C. Bock, C. J. Pelliccione, Y. Li, L. Wu, Y. Zhu, A. C. Marschilok, E. S. Takeuchi, K. J. Takeuchi and F. Wang, *Adv. Energy Mater.*, 2016, **6**, 1502471.
10 J. Coey, A. Berkowitz, L. Balcells, F. Putris and F. Parker, *Appl. Phys. Lett.*, 1998, **72**, 734.
11 H. Duan, J. Gnanaraj and J. Liang, *J. Power Sources*, 2011, **196**, 4779–4784.
12 D. Larcher, C. Masquelier, D. Bonnin, Y. Chabre, V. Masson, J. B. Leriche and J. M. Tarascon, *J. Electrochem. Soc.*, 2003, **150**, A133–A139.
13 P. Poizot, S. Laruelle, S. Grugeon, L. Dupont and J. M. Tarascon, *Nature*, 2000, **407**, 496–499.
14 Q. Q. Xiong, J. P. Tu, Y. Lu, J. Chen, Y. X. Yu, Y. Q. Qiao, X. L. Wang and C. D. Gu, *J. Phys. Chem. C*, 2012, **116**, 6495–6502.
15 S. Komaba, T. Mikumo and A. Ogata, *Electrochem. Commun.*, 2008, **10**, 1276–1279.

16 S. Komaba, T. Mikumo, N. Yabuuchi, A. Ogata, H. Yoshida and Y. Yamada, *J. Electrochem. Soc.*, 2010, **157**, A60–A65.
17 S. Zhu, A. C. Marschilok, E. S. Takeuchi and K. J. Takeuchi, *Electrochem. Solid-State Lett.*, 2009, **12**, A91–A94.
18 S. Zhu, A. C. Marschilok, E. S. Takeuchi, G. T. Yee, G. Wang and K. J. Takeuchi, *J. Electrochem. Soc.*, 2010, **157**, A1158–A1163.
19 M. C. Menard, A. C. Marschilok, K. J. Takeuchi and E. S. Takeuchi, *Electrochim. Acta*, 2013, **94**, 320–326.
20 P. F. Smith, K. J. Takeuchi, A. C. Marschilok and E. S. Takeuchi, *Acc. Chem. Res.*, 2017, **50**, 544–548.
21 A. M. Bruck, C. N. Gannett, D. C. Bock, P. F. Smith, A. C. Marschilok, K. J. Takeuchi and E. S. Takeuchi, *J. Electrochem. Soc.*, 2017, **164**, A6260–A6267.
22 Y. H. Kwon, M. M. Huie, D. Choi, M. Chang, A. C. Marschilok, K. J. Takeuchi, E. S. Takeuchi and E. Reichmanis, *ACS Appl. Mater. Interfaces*, 2016, **8**, 3452–3463.
23 Y. H. Kwon, K. Minnici, M. M. Huie, K. J. Takeuchi, E. S. Takeuchi, A. C. Marschilok and E. Reichmanis, *Chem. Mater.*, 2016, **28**, 6689–6697.
24 Y. Shi, J. Zhang, A. M. Bruck, Y. M. Zhang, J. Li, E. A. Stach, K. J. Takeuchi, A. C. Marschilok, E. S. Takeuchi and G. H. Yu, *Adv. Mater.*, 2017, **29**, 1603922.
25 K. W. Knehr, N. W. Brady, C. N. Lininger, C. A. Cama, D. C. Bock, Z. Lin, A. C. Marschilok, K. J. Takeuchi, E. S. Takeuchi and A. C. West, *ECS Trans.*, 2015, **69**, 7–19.
26 A. Abraham, L. M. Housel, C. N. Lininger, D. C. Bock, J. Jou, F. Wang, A. C. West, A. C. Marschilok, K. J. Takeuchi and E. S. Takeuchi, *ACS Cent. Sci.*, 2016, **2**, 380–387.
27 P. Poizot, S. Laruelle, S. Grugeon, L. Dupont and J. M. Tarascon, *Nature*, 2000, **407**, 496–499.
28 A. S. Andersson, B. Kalska, L. Häggström and J. O. Thomas, *Solid State Ionics*, 2000, **130**, 41–52.
29 J. N. Reimers and J. R. Dahn, *J. Electrochem. Soc.*, 1992, **139**, 2091–2097.
30 T. D. Hatchard and J. R. Dahn, *J. Electrochem. Soc.*, 2004, **151**, A838–A842.
31 I. A. Courtney and J. R. Dahn, *J. Electrochem. Soc.*, 1997, **144**, 2045–2052.
32 L. M. L. Fransson, J. T. Vaughey, R. Benedek, K. Edstrom, J. O. Thomas and M. M. Thackeray, *Electrochem. Commun.*, 2001, **3**, 317–323.
33 C. J. Pelliccione, Y. Ding, E. V. Timofeeva and C. U. Segre, *J. Electrochem. Soc.*, 2015, **162**, A1935–A1939.
34 C. J. Pelliccione, E. V. Timofeeva and C. U. Segre, *Chem. Mater.*, 2015, **27**, 574–580.
35 M. Giorgetti, *ISRN Mater. Sci.*, 2013, **2013**, 1–22.
36 M. Balasubramanian, X. Sun, X. Q. Yang and J. McBreen, *J. Power Sources*, 2001, **92**, 1–8.
37 J. Chouvin, J. Oliver-Fourcade, J. C. Jumas, B. Simon, P. Biensan, F. J. F. Madrigal, J. L. Tirado and C. P. Vicente, *J. Electroanal. Chem.*, 2000, **494**, 136–146.
38 M. D. Sharkov, M. E. Boiko, A. V. Bobyl, E. M. Ershenko, E. I. Terukov and Y. V. Zubavichus, *Crystallogr. Rep.*, 2013, **58**, 993–997.
39 B. H. Toby and R. B. Von Dreele, *J. Appl. Crystallogr.*, 2013, **46**, 544–549.
40 M. J. Newville, *J. Synchrotron Radiat.*, 2001, **8**, 322–324.
41 B. Ravel and M. J. Newville, *J. Synchrotron Radiat.*, 2005, **12**, 537–541.
42 J. Mustre de Leon, J. J. Rehr, S. I. Zabinsky and R. C. Albers, *Phys. Rev.*, 1991, **B44**, 4146.
43 J. J. Rehr, J. Mustre de Leon, S. I. Zabinsky and R. C. Albers, *J. Am. Chem. Soc.*, 1991, **113**, 5135.
44 M. E. Fleet, *Acta Crystallogr.*, 1984, **40**, 1491–1493.
45 E. R. Jette and F. Foote, *J. Chem. Phys.*, 1933, **1**, 29–36.
46 E. A. Owens and E. L. Yates, *Philos. Mag.*, 1933, **15**, 472–488.
47 A. L. Ankudinov, B. Ravel, J. J. Rehr and S. D. Conradson, *Phys. Rev. B: Condens. Matter Mater. Phys.*, 1998, **58**, 7565–7576.
48 A. L. Patterson, *Phys. Rev.*, 1939, **56**, 978–982.
49 H. Liu, G. X. Wang, J. Z. Wang and D. Wexler, *Electrochem. Commun.*, 2008, **10**, 1879–1882.
50 C. N. He, S. Wu, N. Q. Zhao, C. S. Shi, E. Z. Liu and J. J. Li, *ACS Nano*, 2013, **7**, 4459–4469.
51 S. Komaba, T. Mikumo, N. Yabuuchi, A. Ogata, H. Yoshida and Y. Yamada, *J. Electrochem. Soc.*, 2010, **157**, A60–A65.
52 D. C. Bock, K. C. Kirshenbaum, J. Wang, W. Zhang, F. Wang, J. Wang, A. C. Marschilok, K. J. Takeuchi and E. S. Takeuchi, *ACS Appl. Mater. Interfaces*, 2015, **7**, 13457–13466.
53 A. J. Bard and L. R. Faulkner, *Electrochemical Methods: Fundamentals and Applications*, Wiley, New York, 2000.
54 K. He, J. Li, X. Yu, Q. Meng, E. Hu, K. Sun, X.-Q. Yang, Y. Zhu, H. Gan, A. Stach Eric, D. Su, S. Zhang, H. Yun, B. Murray Christopher, Y. Zhu and Y. Mo, *Nat. Commun.*, 2016, **7**, 11441.
55 M. R. Nadler and C. P. Kempter, *Anal. Chem.*, 1959, **31**, 2109.
56 S. Permien, S. Indris, U. Schürmann, L. Kienle, S. Zander, S. Doyle and W. Bensch, *Chem. Mater.*, 2016, **28**, 434–444.
57 K. W. Knehr, N. W. Brady, C. A. Cama, D. C. Bock, Z. Lin, C. N. Lininger, A. C. Marschilok, K. J. Takeuchi, E. S. Takeuchi and A. C. West, *J. Electrochem. Soc.*, 2015, **162**, A2817–A2826.
58 N. W. Brady, K. W. Knehr, C. A. Cama, C. N. Lininger, Z. Lin, A. C. Marschilok, K. J. Takeuchi, E. S. Takeuchi and A. C. West, *J. Power Sources*, 2016, **321**, 106–111.
59 K. W. Knehr, C. A. Cama, N. W. Brady, A. C. Marschilok, K. J. Takeuchi, E. S. Takeuchi and A. C. West, *Electrochim. Acta*, 2017, **238**, 384–396.
60 R. K. Hocking, R. Brimblecombe, L.-Y. Chang, A. Singh, M. H. Cheah, C. Glover, W. H. Casey and L. Spiccia, *Nat. Chem.*, 2011, **3**, 461–466.
61 C. Lamberti, C. Prestipino, F. Bonino, L. Capello, S. Bordiga, G. Spoto, A. Zecchina, S. Diaz Moreno, B. Cremaschi, M. Garilli, A. Marsella, D. Carmello, S. Vidotto and G. Leofanti, *Angew. Chem., Int. Ed.*, 2002, **41**, 2341–2344.
62 J. J. Rehr and R. C. Albers, *Rev. Mod. Phys.*, 2000, **72**, 621–654.
63 J. J. Rehr and A. L. Ankudinov, *Coord. Chem. Rev.*, 2005, **249**, 131–140.
64 A. M. Beale and B. M. Weckhuysen, *Phys. Chem. Chem. Phys.*, 2010, **12**, 5562–5574.
65 S. Calvin, S. X. Luo, C. Caragianis-Broadbridge, J. K. McGuinness, E. Anderson, A. Lehman, K. H. Wee, S. A. Morrison and L. K. Kurihara, *Appl. Phys. Lett.*, 2005, **87**, 233102.
66 S. Calvin, M. M. Miller, R. Goswami, S.-F. Cheng, S. P. Mulvaney, L. J. Whitman and V. G. Harris, *J. Appl. Phys.*, 2003, **94**, 778–783.

67 A. I. Frenkel, C. W. Hills and R. G. Nuzzo, *J. Phys. Chem. B*, 2001, **105**, 12689–12703.
68 F. Jiménez-Villacorta, A. Muñoz-Martín and C. Prieto, *J. Appl. Phys.*, 2004, **96**, 6224–6229.
69 V. V. Srabionyan, A. L. Bugaev, V. V. Pryadchenko, L. A. Avakyan, J. A. van Bokhoven and L. A. Bugaev, *J. Phys. Chem. Solids*, 2014, **75**, 470–476.
70 D. C. Bock, C. Pelliccione, K. W. Knehr, J. Wang, W. Zhang, F. Wang, J. Wang, A. C. West, A. C. Marschilok, K. J. Takeuchi and E. S. Takeuchi, *ACS Appl. Mater. Interfaces*, 2016, **8**, 11418–11430.
71 Y. Zhang, C. J. Pelliccione, A. B. Brady, H. Guo, P. F. Smith, P. Liu, A. C. Marschilok, K. J. Takeuchi and E. S. Takeuchi, *Chem. Mater.*, 2017, **29**, 4282–4292.
72 C. A. Cama, C. J. Pelliccione, A. B. Brady, J. Li, E. A. Stach, J. Wang, J. Wang, E. S. Takeuchi, K. J. Takeuchi and A. C. Marschilok, *Phys. Chem. Chem. Phys.*, 2016, **18**, 16930–16940.
73 J. A. Varnell, E. C. M. Tse, C. E. Schulz, T. T. Fister, R. T. Haasch, J. Timoshenko, A. I. Frenkel and A. A. Gewirth, *Nat. Commun.*, 2016, **7**, 12582.
74 A. Frenkel, *Z. Kristallogr.*, 2007, **222**, 605–611.
75 A. I. Frenkel, *J. Synchrotron Radiat.*, 1999, **6**, 293–295.

